ACSNANO

www.acsnano.org

ARTICLE

Remote Lightening and Ultrafast Transition: Intrinsic Modulation of Exciton Spatiotemporal Dynamics in Monolayer MoS_2

Pengfei Qi,[#] Yang Luo,[#] Wei Li, Yang Cheng, Hangyong Shan, Xingli Wang, Zheng Liu, Pulickel M. Ajayan, Jun Lou, Yanglong Hou, Kaihui Liu, and Zheyu Fang*

Cite This: https://dx.doi.org/10.1021/acsnano.0c01165

Read Online

ACCESS | Metrics & More | Article Recommendations | Supporting Information

ABSTRACT: Devices operating with excitons have promising prospects for overcoming the dilemma of response time and integration in current generation of electron- or/and photon-based elements and devices. Although the intrinsic properties including edges, grain boundaries, and defects of atomically thin semiconductors have been demonstrated as a powerful tool to adjust the bandgap and exciton energy, investigating the intrinsic modulation of spatiotemporal dynamics still remains challenging on account of the short exciton diffusion length. Here, we achieve the attractive remote lightening phenomenon, in which the emission region could be far away (up to 14.6 μm) from the excitation center, by utilizing a femtosecond laser with ultrahigh peak power as excitation source and the edge region with high photoluminescence efficiency as a bright emitter. Furthermore, the ultrafast transition between exciton and trion is demonstrated, which provides insight into the intrinsic modulation on populations of exciton and trion states. The complete cascaded physical scenario of exciton spatiotemporal dynamics is eventually established. This work can refresh our perspective on the spatial nonuniformities of CVD-grown atomically thin semiconductors and provide important implications for developing durable and stable excitonic devices in the future.

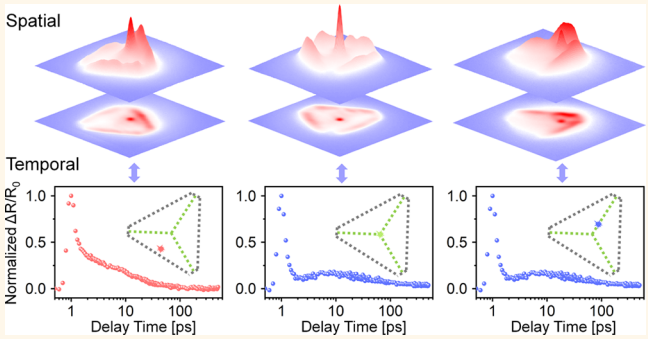

KEYWORDS: *molybdenum disulfide, grain boundary, exciton flux, remote lightening, ultrafast transition*

Electrons and photons, carriers of energy and information, are of central importance in current generation of optoelectronic elements and devices. However, electrons as charged particles are sensitive to the surroundings because of strong Coulomb interactions, leading to the bottleneck of nanosecond response time for integrated electric devices.[1] Although the operation speed of semiconductor-based optoelectronic components can exceed several gigahertz *via* manipulating photons, the high integration of photonic devices is challenging due to the optical diffraction limit.[2] Excitons, or bound electron−hole pairs, which are hydrogen-like bosonic quasiparticles with a Bohr radius of nanometer dimensions, potentially combining advantages of electrons and photons, can efficiently interconnect photonic and electronic systems.[3] Therefore, various functional devices operating with excitons including modulators, storage devices, field-gradient devices, and transistors have been envisaged and demonstrated in bulk semiconductor-based coupled quantum wells in past decades.[4−9] However, the low temperature required for operation limits their practical application.

The emergence of atomically thin transition metal dichalcogenides (TMDs) has attracted significant interest to pursue excitonic devices for two major reasons. On one hand, owing to the reduced dielectric screening, enhanced Coulomb interactions, and relatively large effective masses of charge carriers, the electron−hole pairs formed in monolayer TMDs have ∼1 nm Bohr radius and ∼500 meV binding energy, over an order of magnitude larger than conventional semiconductors, enabling the manipulation of exciton at room temperature.[10−14] On the other hand, the time-reversal symmetry, broken inversion symmetry, and strong spin−orbit splitting in monolayer TMDs provide an alternative steerable

Received: February 10, 2020
Accepted: June 3, 2020
Published: June 3, 2020

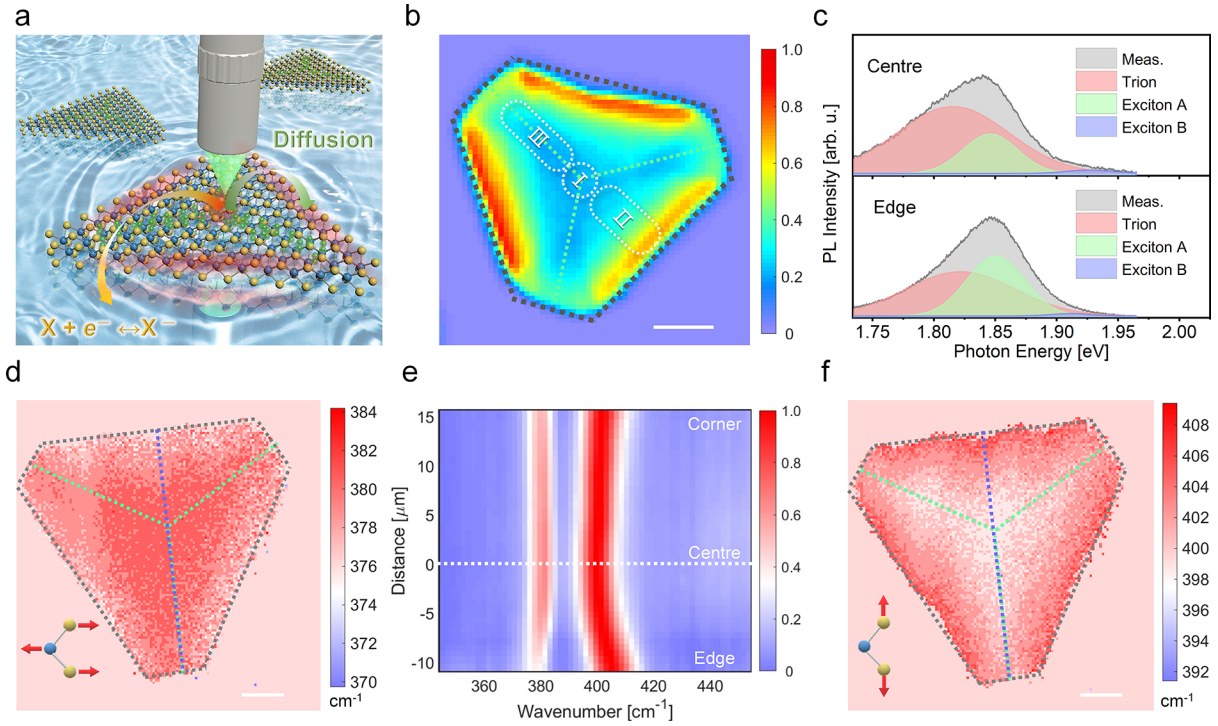

Figure 1. Intrinsic modulation of GBs and edges on electronic and photonic properties. (a) Schematic of the intrinsic modulation of exciton spatiotemporal dynamics in monolayer MoS_2. (b) PL intensity maps of CVD-grown monolayer MoS_2. The excitation sites chosen in this work are divided into three regions: center (I), near edge (II), and on GBs (III). (c) Representative PL spectra obtained from the edge region and center region. (d and f) Micro-Raman spectroscopic maps plotting (d) E^1_{2g} peak frequency and (f) A_{1g} peak frequency of CVD-grown monolayer MoS_2. Inset: Schematic atomic displacement of the in-plane E^1_{2g} and out-of-plane A_{1g} modes. (e) Micro-Raman spectra (average of the sites within 1.25 μm) along the blue dotted lines in (d) and (f). Scale bars are 5 μm.

degree of freedom, valley pseudospin, which can be utilized for information storage and processing and thereby renovate modern charge- and spin-based technologies.[15−21]

The necessary step toward exciton devices is the control of exciton spatiotemporal dynamics including relaxation and transport. The strain,[22,23] electric field,[24,25] electron-doping,[20] and local dielectric environment[26] have been demonstrated as effective methods to modulate exciton flux theoretically and experimentally in recent years. However, the intrinsic modulation of edges, grain boundaries (GBs), and defects on exciton dynamics has not caught extensive attention for chemical vapor deposition (CVD)-grown monolayer TMDs. The spatial nonuniformities arising from edges, GBs, and defects have been treated as fatal shortcomings, and thereby their adverse impacts on exciton emission efficiency were mainly of concern.[27,28] Compared with monolayer TMDs exfoliated from bulk crystals, CVD-grown monolayer TMDs have greater prospects for device applications, where the low cost, high yield, large area, and repeatable and controllable production are required. The GBs or defects engineering can complement or surpass strain and electric technologies for modulating exciton flux in future excitonic devices, especially in the scenario in which durability and stability are vital.[29]

Here, the intrinsic modulation of GBs on exciton spatiotemporal dynamics of CVD-grown monolayer MoS_2 was studied. The attractive remote lightening phenomenon—emission locations could be tens of micrometers away from the optical excitation center—was observed. Supported by numerical calculations based on the spatial-temporal dynamic model, the underlying mechanism related to exciton diffusion and the giant modulation of GBs on PL efficiency was discussed. Furthermore, the high electron-doped concentration near the GB region has a great influence on the temporal evolution of the exciton, where the ultrafast transition between exciton (X) and trion (X^-) occurs. This work provides important implications for designing stable and durable excitonic devices such as exciton guides, couplers, and isolators based on GB engineering in CVD-grown TMDs.

RESULTS AND DISCUSSION

Intrinsic Modulation of GBs and Edges on Electronic and Photonic Properties. The monolayer MoS_2 used in experiments was directly grown on a silicon/silica substrate by CVD methods. The monolayer MoS_2 could be confirmed by microscopy and PL spectroscopy. All the measurements reported here were performed at room temperature. An illustration of the intrinsic modulation of exciton dynamics is shown in Figure 1a. Under the excitation of a pulsed laser, excitons experience spatiotemporal relaxations. Combining confocal optical microscopy with spectrography, the excitation laser (continuous wave, 532 nm) was scanned over the sample and the PL emission spectra at different sites were recorded. Figure 1b shows the spatial distribution of PL spectrum integrals over the emission wavelength. In CVD-grown triangle MoS_2 flakes, the GBs tend to exhibit as interconnected straight lines with turning angles of 120°.[28] Here the GBs among three triangular grains can be clearly observed owing to the excited-state quenching.[27] Extracting spectra from Figure 1b, it can be found that the population ratio of exciton to trion state decreases, while the peaks red shift (9 meV for exciton and trion) from edge to GB (see Supporting Note S1 for more details).

https://dx.doi.org/10.1021/acsnano.0c01165
ACS Nano XXXX, XXX, XXX−XXX

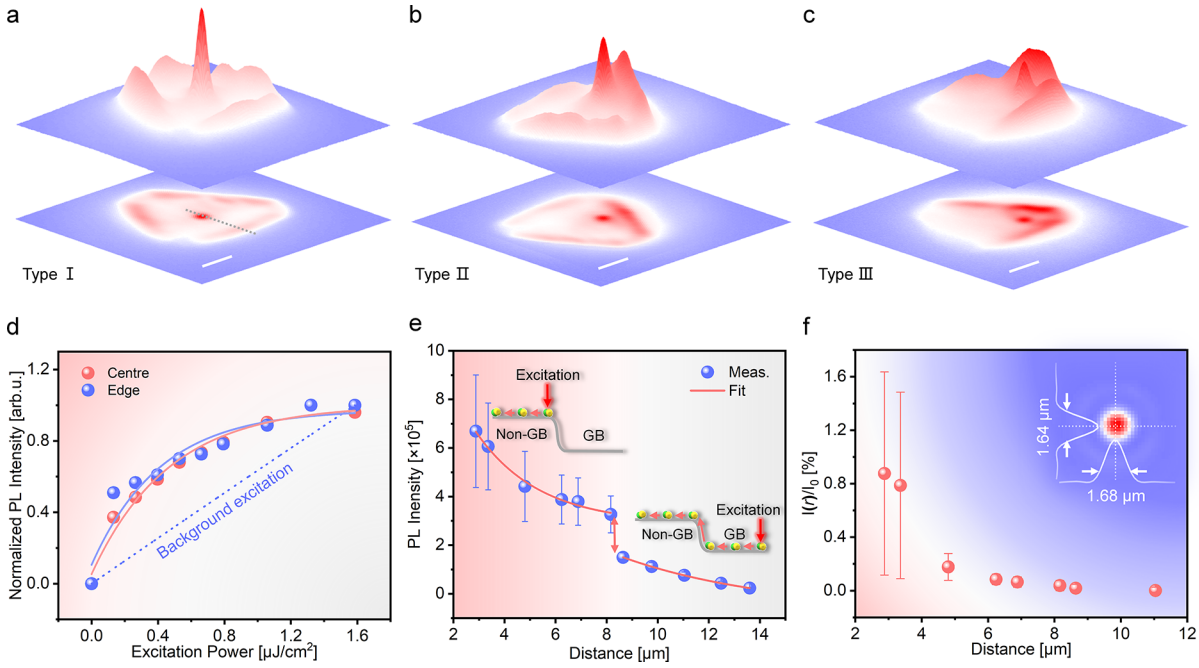

Figure 2. Remote lightening of edges *via* exciton flux. (a–c) Three typical cases of spatial emission profiles recorded by EMCCD, corresponding to the three regions in Figure 1b. (d) Dependence of PL intensity in the center and edge region on excitation power. The dependence of PL intensity in the edge region can be estimated as the blue dotted line for background excitation. (e) Average emission intensity in the edge region of 2 μm × 4 μm as a function of the distance *r* from the excitation center to the selected region. The insets depict the physical scenario of the excitation center in a non-GB (left) and a GB (right). (f) Spatial intensity profiles of an excitation laser beam in the inset figure. Scale bars are 5 μm.

Moreover, we note that the population ratios of exciton to trion state for the edge and center exhibit a more evident difference in the PL spectra excited by a femtosecond laser, which possess extremely high peak intensity. As depicted in Figure 1c, the femtosecond laser (408 nm) excited PL spectra of the edge and center can be well fitted by three peaks deriving from the radiative recombination of exciton B (is not considered in this work), exciton A (is called an exciton in the text), and trion states. It is clear that the shape of PL spectra changes greatly from edge to center due to the decreasing ratio of exciton to trion intensities. It can be concluded that the increased relative emission of the trion is correlated with a reduction in the overall PL intensity for the interior GB region, which is consistent with ref 27. Here the decreased population ratio of exciton to trion state for the GB region can be attributed to the transition between exciton and trion, which is determined by electron-doped concentration.

To obtain spatially resolved electron-doped concentration distributions for monolayer MoS_2 flakes, micro-Raman mapping was performed. Monolayer MoS_2 has a typical Raman spectrum with two dominant peaks at 376.7 and 404.4 cm^{-1}, corresponding to atomic displacement of the in-plane E^1_{2g} and out-of-plane A_{1g} modes, respectively (see Supporting Note S2).[30] Figure 1d and f show the Raman mappings of the E^1_{2g} and A_{1g} shift. The Raman spectra of GB regions exhibit an obvious red shift for the A_{1g} peaks as well as a slight blue shift for the E^1_{2g} peak compared with edge regions, and therefore the three GBs were distinguished in Figure 1d and f. For clarity, the Raman spectra of the sites along the blue dotted line in Figure 1d and f were extracted and plotted in Figure 1e. It can be seen that the shift range is about 5.5 cm^{-1} for the A_{1g} peak, while it is about 2 cm^{-1} for the E^1_{2g} peak (see Supporting Note S2 for more details). The obvious red shift of the A_{1g} peak for GB regions compared with edge regions indicates that GB regions have a higher electron-doped concentration than edge regions,[31] which may induce a significant transition from exciton to trion and an increased population ratio of trion to exciton states in GB regions. The transition occurs on the scale of picoseconds according to our time-resolved differential reflection measurements, which will be discussed later.

Remote Lightening of Edges *via* Exciton Flux. To explore the modulation of GBs on exciton flux in the CVD-grown monolayer MoS_2, the direct PL imaging technique was adopted, which is a more direct way compared with the PL mapping because the latter only records the PL intensity at the excitation center.[20,24,32,33] The femtosecond laser was focused on the different sites of monolayer MoS_2 to pump excitons, which undergo ultrafast Auger recombination and then diffuse along the pathway modulated by intrinsic spatial nonuniformities. Generally speaking, the ultralow exciton density after the transport distance exceeding the short diffusion length makes verifying the intrinsic modulation on exciton flux in monolayer MoS_2 challenging. Fortunately, various studies have demonstrated that the exciton diffusion length can be enhanced significantly by increasing the laser power.[25,34] It has been reported that the effective diffusion coefficient remains nearly constant (~0.2 cm^2/s) in the low-density regime and strongly increases above 40 cm^2/s at higher densities in monolayer WSe_2 under the excitation of 100 fs laser pulses,[34] which may lead to the observable exciton diffusion in monolayer TMDs. Therefore, in our micro-PL imaging experiments, the femtosecond laser with high peak power (ensuring an energy density of ~10 $\mu J/cm^2$) was chosen as the excitation source. At such high power levels, the thermal and renormalization effects can be reasonably neglected (see Supporting Note S3 for more details). Moreover, the edge region that has a higher PL

https://dx.doi.org/10.1021/acsnano.0c01165
ACS Nano XXXX, XXX, XXX−XXX

efficiency was chosen as a bright emitter to detect the exciton flux after propagating a long distance, inspired by ref 23, which utilized the exposed WSe_2 that extends out of the heterostructure as a bright emitter to monitor the interlayer exciton flux modulated by the electric field.

The exciton transport and recombination with bright radiation of the MoS_2 flake can be recorded simultaneously using an electron-multiplying charge-coupled device (EMCCD) camera. The acquired spatial emission profiles enable us to track the exciton flux modulated by GBs. The spatial emission profiles of different excitation sites along the midperpendicular of the triangle-shaped MoS_2 (such as the blue dotted lines in Figure 1d and f) were studied. Surprisingly, the sample edges that are far away from the excitation center could be lightened through exciton flux. These profiles can be divided into three typical cases, as shown in Figure 2a−c. First, when the excitation laser was focused on the intersection region I of three GBs (Figure 1b and Supporting Figure S5), the radiation intensities of three edge regions are approximately the same, as depicted in Figure 2a. Second, when the excitation site was located at region II near the edge (Figure 1b and Figure S5), the spatial emission profiles of the three edge regions contain a relativelt brighter edge and two darker edges, as depicted in Figure 2b. Third, when the excitation pulses were focused on GB region III (Figure 1b and Figure S5), the spatial emission profile exhibits a relatively darker edge and two brighter edges, as depicted in Figure 2c. It should be noted that the remote lightening of edges is ubiquitous for our sample (see Supporting Note S5 for more details).

The remote lightening of edges (~5 μm away from the excitation center) is an unusual phenomenon in monolayer TMDs, and therefore, a further confirmation was performed. The excitation light has been removed by the filter, and the influence of the optical system can be excluded by taking the WSe_2 as a reference (see Supporting Note S6.). To exclude the possibility that the signal was from the background excitation of the laser, the dependences of PL intensities for the center region and edge region on excitation power were measured (see Supporting Movie S1). The normalized experimental results and fitted curves are depicted in Figure 2d. Providing the background intensity is only 1% (greater than the data in Figure 2f) of the center intensity for the excitation laser, the dependence of the PL intensity for the edge region can be estimated as the blue dotted line supposing that the lightening edges come from background excitation. It is completely different from experimental results, and thereby the background excitation can also be ruled out.

To quantitatively evaluate the farthest distance of remote lightening, the monolayer MoS_2 flake with a larger size was excited by the femtosecond laser with the energy density of 4 $\mu J/cm^2$. Similarly, the spatial PL emission profiles for different excitation sites along the midperpendicular were recorded (see Supporting Movie S2). From EMCCD images, we obtained the average emission intensity in an edge region of 2 μm × 4 μm (white dotted closed region in Supporting Movie S2) as a function of the distance r from the excitation center to the selected region center, as illustrated in Figure 2e. The scatter points in Figure 2e could be fitted by two-stage exponential decay curves, and the discontinuous site appears at r = 8 μm. It can be estimated that the detection limit of 3σ (σ is the standard deviation of the background level) is reached at about r = 14.6 μm for remote lightening. There is no analogous discontinuity on the spatial intensity profiles (normalized by the center intensity I_0) of the excitation laser point (Figure 2f), which further excludes the remote lightening arising from background excitation. As previously reported, the GBs appear as interconnected straight lines with turning angles of 120°, and the intersection region of three GBs approximately overlaps with the center of equilateral triangle MoS_2 monolayer flakes.[27,28,35] It can be easily proved from geometric calculation that the discontinuous site is exactly located in the intersection region of three GBs, that is, the dividing point of GBs and non-GBs.

Physical Scenario of Remote Lightening. Considering the large effective diffusion coefficient under femtosecond laser excitation and the significant difference of PL efficiency between edges and GBs, the remote lightening behaviors are speculated as following a physical scenario: excitons are produced by femtosecond laser flow toward the edges of the sample owing to temperature and concentration gradients and then recombine with bright radiation. A quantitative discussion on the underlying mechanism of remote lightening is presented below. Figure 3a shows the dependence of PL intensity on excitation energy density at different sites (marked with the same color in the inset schematic of Figure 3b). It is clearly evident that there is a significant difference between GB regions and edge regions, which are almost the same for the sites on the GB. Meanwhile, the experimental data of each excitation site could be fitted by exponential decay curves (plotted with the same color in Figure 3a), and the PL saturation intensity of different sites was extracted and plotted in Figure 3b (normalized by the saturation intensity of the center). It can be observed that the PL saturation intensity near the edge is nearly 7-fold (maybe larger for the edge region) higher than that of the GB region, while in the excitation center, the excitons with an ultrahigh density undergo an ultrafast Auger recombination and a large amount of excitons (nearly 90% according to Figure 4a−c) annihilate without radiation. Therefore, the emission efficiency per exciton of the edge region can be 2 orders larger than that of the GB region, which enables us to detect the low-density exciton flux.

The spatial-temporal distribution of exciton density during the diffusion process can be described by a spatial-temporal dynamic model (see Supporting Note S6):

$$N(x, t) = \frac{N_0}{\sqrt{\pi w^2(t)}} \exp\left(-\frac{x^2}{w^2(t)} - \frac{t}{\tau}\right) \quad (1)$$

where x *is* the distance to the excitation center, N_0 is the initial exciton density induced by excitation pulses, $w(t) = \sqrt{w_0^2 + 4Dt}$ is the width of the spatial distribution of exciton density, w_0 is the width of the excitation beam, D is the effective diffusion coefficient, and τ is the lifetime of the exciton. The theoretical spatial distribution of the exciton density can be obtained by the integral of $N(x, t)$ over time. The blue points in Figure 3c show the spatial emission profile along the gray dotted line in Figure 2a. Combining with the emission efficiency per exciton and the instrument response function (green curve in Figure 3c), the spatial emission profile was quantitatively reproduced by the spatial-temporal dynamic model, as depicted in Figure 3c (see Supporting Note S8 for more details). The laser width w_0 = 0.7 μm, the effective diffusion coefficient D = 40 cm^2/s, and the exciton lifetime τ = 250 ps were adopted in the quantitative simulation. It should

https://dx.doi.org/10.1021/acsnano.0c01165
ACS Nano XXXX, XXX, XXX−XXX

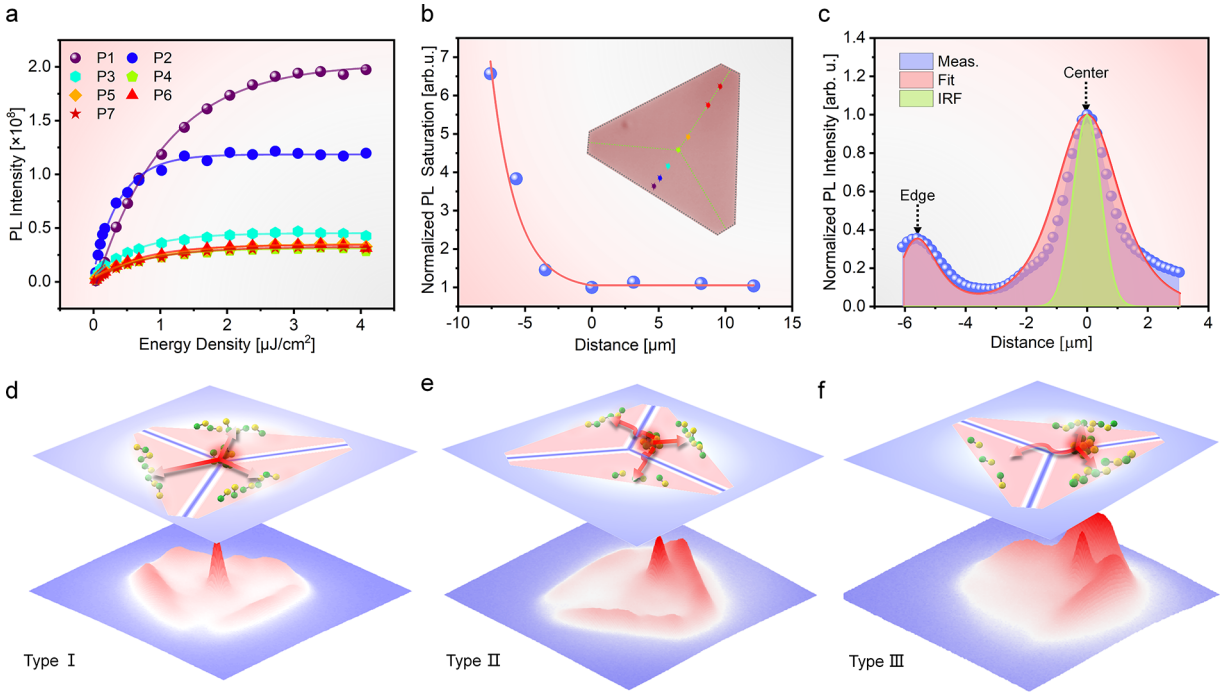

Figure 3. Physical scenario of remote lightening. (a) Dependence of PL intensity on excitation energy density at different sites (marked with the same color in the inset of (b)). (b) PL saturation intensity of different sites extracted from (a). (c) Quantitative simulation of the spatial emission profile based on the simple spatial-temporal dynamic model. (d–f) Physical scenario of three typical spatial emission profiles corresponding to Figure 2a–c.

be noted that the femtosecond laser power should be high enough to ensure that the exciton radiation can be detected by EMCCD even for the farthest region from the excitation center. Therefore, the choice of femtosecond laser peak power depends on the sensitivity of the camera and the efficiency of the optical system. Under our experimental conditions, it can be established that the energy density should be on the scale of 10 μJ/cm^2 to obtain the effective diffusion coefficient of ~10 cm^2/s according to ref 34.

Considering the reduced bandgap on GBs,[29] we can understand the complicated questions of how the three typical spatial emission profiles (Figure 2a–c) can be induced by the modulated exciton flux and why the discontinuous site appears at the dividing point of GB and non-GB. As shown in Figure 3d, when the excitation laser was focused on the intersection region of three GBs, the triple rotation symmetry of the system determines the excitons equally flow to the three edges, which leads to approximately the same radiation intensity in the three edges (Figure 2a). Provided that the excitation site was located at the region near one edge, excitons that arrived at two distant edges experienced a longer distance and an additional potential well, which seriously impeded its diffusion because of the funnel effect (Figure 3e).[22] Thus, the two edges are darker than another edge in Figure 2b. Lastly, when the excitation laser was focused on the GB, the excitons need to go through a potential barrier to reach the distant edge (Figure 3f). Hence excitons tend to flow to the nearest edge, and the spatial emission profile of Figure 2c can occur naturally. Additionally, as shown in the insets of Figure 2e, excitons diffused to edge region should leap over an additional potential barrier for the excitation center in the GB region (right inset) compared with that for the excitation center in the non-GB region (left inset). Therefore, there is an extreme descent for the emission intensity in the selected edge region by changing the excitation center from non-GB region to GB region (Figure 2e). Consequently, the remote lightening can be reasonably attributed to the exciton flux modulated by GBs and edges.

Note that the simplified analytical exciton diffusion model presented in this work can quantitatively explain the remote lightening of the edge, but fails to reproduce three typical cases of spatial emission profiles (Figure 2a–c) modulated by GBs, because the influence of spatial inhomogeneity on the diffusion was not considered in the model. As supplementary, the qualitative physical scenario was presented to explain how the three typical cases of spatial emission profiles can be induced by GBs. It is assumed that some of the excitons can survive traveling through areas of grain boundaries, which could be a large obstacle for the exciton's transit due to funneling effects generated from reduced electronic gaps and a high electron-doped concentration. The hypothesis can be supported by three reasons. First, from the aspect of barrier energy, based on the schematic diagram explaining the funnel effect depicted in ref 36, the reduced exciton energy induced by GBs can be estimated as 9 meV from the red shift of the exciton peak (see Supporting Note S2 for more details), which is far less than the thermal fluctuation of $k_BT \approx 26$ meV at room temperature. This means that excitons are very likely running away from the funnel effect of GBs owing to thermal fluctuation. Second, from the aspect of barrier spatial width, the spatial scale that the electronic gap deeply modulated by GBs is less than 5 nm by the measurement of scanning tunneling microscopy,[29] which will further increase the exciton survival probability to travel through GBs owing to quantum tunneling. Lastly, from the aspect of exciton transition, although the grain boundaries full of free carriers will facilitate the transition from excitons to trions, some of the trions will reconvert to excitons and electrons when they reach the non-GB region with ultralow electron-doped concentration. The above complicated physics

https://dx.doi.org/10.1021/acsnano.0c01165
ACS Nano XXXX, XXX, XXX–XXX

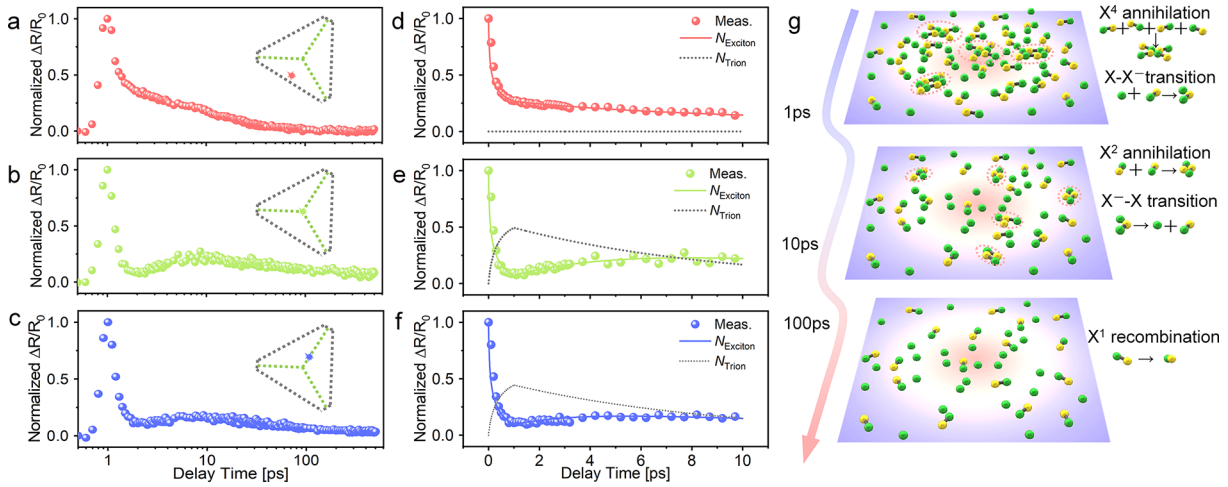

Figure 4. Ultrafast transition between exciton and trion. (a–c) Time-resolved differential reflection signals $\Delta R/R_0$ (normalized by the peak values) for the pump and probe pulses focused on the edge region, center region, and GB region. The actual time was increased by 1 ps on the timelines, and the inset schematics show the specific excitation sites. (d–f) Enlarged figures of the first 10 picoseconds corresponding to (a)–(c). (g) Schematic diagram of the complete physical scenario of exciton spatiotemporal dynamics.

of exciton traveling through GBs deserves further investigation by ultrafast and super-resolution technologies, which might be temporally out of the main scope of the current work.

Ultrafast Transition between Exciton and Trion. Besides supporting the explanation of remote lightening behavior, the femtosecond pump–probe technique also is a powerful tool to clarify the intrinsic modulation on the populations of exciton and trion states within a femtosecond–picosecond time scale. In our ultrafast measurements, in order to pump and probe the excitons in monolayer MoS_2 flakes, the wavelength of the pump pulse was fixed at 408 nm, while the probe was chosen as 660 nm. The pump and probe energy densities were 6.0 and 0.2 $\mu J/cm^2$, respectively.

Figure 4a shows the normalized differential reflection signal $\Delta R/R_0$ when the pump and probe pulses were focused on the edge region (red point in the inset of Figure 4a). Note that the timeline is in log coordinates to clearly present the details of the transient signal on a large time span (−800 fs to 500 ps) and the actual time was increased by 1 ps to avoid mathematical invalidity. It can be found that the high-density excitons pumped by femtosecond pulses (the rising edge of $\Delta R/R_0$) undergo three decay processes: multiexciton annihilation ($\sim N^x$, where $x > 2$ and $x = 4$ was demonstrated in previous studies),[37] exciton–exciton annihilation ($\sim N^2$), and single exciton recombination ($\sim N$). The exciton relaxation dynamics on the first 10 picoseconds is enlarged and depicted in Figure 4d. It is clearly evident that the fast multiexciton annihilation (0–1 ps) and relative slower exciton–exciton annihilation (>1 ps) are dominant during this stage.

When coaxial pump and probe pulses were focused on the intersection site of three GBs (green point in the inset of Figure 4b) and on the site of the GB (blue point in the inset of Figure 4c), the ultrafast signals were plotted in Figure 4b and c, and the corresponding enlarged figures of the first 10 picoseconds are depicted in Figure 4e and f, respectively. Surprisingly, the transient differential reflection signals of Figure 4e and 4f go through a dramatic reduction within the first picosecond and then slightly increase with the delay time. Since the amplitude of $\Delta R/R_0$ is proportional to the pumped exciton density,[38] the rapidly dropping amplitude means the appearance of a new exciton relaxation channel, while the subsequent increasing implies the emergence of an additional channel that can produce excitons in the monolayer MoS_2. The tremendous changes of relaxation dynamics in the edge and GBs remind us of the intrinsic modulation on the electron-doped concentration mentioned above, which is closely related to the generation and decomposition of the trion.

The ultrafast transition between exciton and trion provides a reasonable interpretation for the anomalous changes of relaxation dynamics. Integrating the generation and decomposition of the trion into the common rate equation, the modified rate equations that describe the exciton and trion dynamics on the first 10 picoseconds can be written as the following:

$$\frac{\partial N}{\partial t} = -\mathcal{A}N^4 - \mathcal{B}N^2 - C(N_e - N_T)N + \mathcal{D}N_T \quad (2a)$$

$$\frac{\partial N_T}{\partial t} = C(N_e - N_T)N - \mathcal{D}N_T \quad (2b)$$

where N and N_T are the exciton and trion density, respectively; N_e is the electron-doped concentration in different sites of monolayer MoS_2, $\mathcal{A}$ and $\mathcal{B}$ are the four exciton annihilation rate and exciton–exciton annihilation rate, C is the transition rate from exciton and electron to trion, and $\mathcal{D}$ is the decomposition rate from trion to exciton and electron. It should be noted that the exciton diffusion and the radiative recombination of exciton and trion can be neglected during the first 10 picoseconds.

The differential eqs 2a and 2b can be numerically solved using the Runge–Kutta method, and the ultrafast signals depicted in Figure 4d–f can be well fitted by the modified rate equations. Besides, the corresponding trion density evolution on the first 10 picoseconds was also plotted as gray dotted lines in each figure (see Supporting Note S9 for more details). The electron-doped concentrations N_e adopted in the fitting process are 10^{11} and 0.85×10^{11} cm^{-2} for Figure 4e and f, respectively, and the ultrafast transition between exciton and trion cannot be ignored, which is consistent with the results of Raman mappings (Figure 1d–f). Therefore, it can be concluded that the ultrafast transition between exciton and trion in the CVD-grown monolayer MoS_2 flake is demon-

https://dx.doi.org/10.1021/acsnano.0c01165
ACS Nano XXXX, XXX, XXX–XXX

strated by the femtosecond pump−probe technique, which provides a clearer physical scenario for the intrinsic modulation on the populations of exciton and trion states (see Supporting Note S10 for the analysis of other excitation sites). The excitons transiting to trions in the high electron doped GB region results in a lower PL efficiency compared with the edge region.

Lastly, the complete cascaded physical scenario of exciton spatiotemporal dynamics could be summarized as in Figure 4g. The four-exciton (X^4) annihilation and the transition from exciton (X) to trion (X^-) is dominant in the first picosecond (top diagram). In the following tens of picoseconds, the decomposition from trion to exciton competes with exciton−exciton (X^2) annihilation (middle diagram). And then the exciton diffusion and single-exciton (X^1) recombination (bottom diagram) mainly occur in hundreds of picoseconds to nanoseconds.

CONCLUSIONS

In conclusion, the intrinsic modulation of GBs and edges on exciton spatiotemporal dynamics in CVD-grown monolayer MoS_2 was investigated with micro-PL imaging and femtosecond pump probe techniques. The complete cascaded physical scenario of exciton spatiotemporal dynamics was elaborately established. The significant remote lightening phenomenon in which the emission region could be far away (up to 14.6 μm) from the optical excitation center was observed. The underlying mechanism was demonstrated as the cooperation of exciton diffusion and the giant modulation of GBs and edges on PL efficiency based on the simple spatial-temporal dynamic model. Considering the ultrafast transition between exciton and trion, the modified relaxation rate equations quantitatively explained the anomalous behavior of ultrafast signals in the GB regions, which provides insight into the intrinsic modulation on the populations of exciton and trion states. This work can refresh our perspective on the spatial nonuniformities arising from edges, GBs, and defects for CVD-grown monolayer TMDs and provides us an important inspiration that GB or defect engineering could be a powerful tool to modulate exciton flux in future durable and stable excitonic devices such as exciton guides, couplers, and isolators. Moreover, the GB or defect engineering might be an effective and simple method to manipulate excitons and realize promising exciton behaviors such as exciton Hall effects,[33] exciton liquids,[39] and Bose−Einstein condensation of excitons.[40]

MATERIALS AND METHODS

Sample Preparations. The MoS_2 monolayers were synthesized by the CVD method: MoO_3 nanoribbons were fabricated through dissolving sodium molybdate (Na_2MoO_4) in nitric acid and then transferring the solution to a Teflon container at 170 °C. The MoO_3 ribbons were cut into pieces and placed on a silicon base. In the quartz tube, bare Si/SiO_2 substrates with a SiO_2 thickness of 540 nm were placed on each side of the silicon substrate with MoO_3, and 0.8 g of sulfur was placed on the side of the N_2 inlet port. The tube was inserted into a furnace and gradually heated to a temperature of 550 °C to evaporate sulfur, with N_2 flowing through the tube at 200 sccm. After heating to 850 °C and holding for 10−15 min, MoS_2 flakes were formed, and the chamber was cooled back to room temperature.[41]

Confocal Raman and PL Spectrum Measurements. Raman and PL mappings were performed by a confocal micro-Raman spectrometer (Horiba XploRA PLUS), employing an excitation laser with a wavelength of 532 nm. The Raman spectra were detected with a 100× objective lens (Olympus MPlan N, NA = 0.9) and 1800 mm^{-1} grating for high spatial and spectral resolution, while for the PL spectrum, a 600 mm^{-1} grating was used for high intensity.

Mirco-PL Imaging. The schematic of the mirco-PL imaging apparatus is presented in Figure S10. The femtosecond pulses (817 nm, 73 fs, 80 MHz) emitted from a mode-locked oscillator (Tsunami 3941C-25XP) were focused into a photonic crystal fiber (Newport SCG-800) to generate supercontinuum white light. The pump pulses were selected by a 600 ± 10 nm bandpass filter (Thorlabs FB600-10) and then focused by an infinity-corrected long working distance micro-objective (Mitutoyo, 100×) to excite the monolayer MoS_2. For spatial imaging, a 650 nm long-pass edge filter (Thorlabs FEL0650) was used to block excitation light. The filtered light was imaged by an EMCCD camera (Andor Ixon 897) with the micro-objective and matched wide-field tube lens (Thorlabs TTL200-A). For spectral measurements (Figure 1c), the filtered light was coupled to a spectrometer (Acton SP2500) equipped with a liquid nitrogen cooled CCD. The homemade apparatus is convenient for switching between spectral measurement and spatial imaging by the removable right-angle silver mirror in the cage cube.

Ultrafast Measurements. Ultrafast pump−probe measurements in the reflection configuration were carried out. Detailed descriptions of our home-built apparatus can be found in a previous work.[42] The femtosecond pulses (817 nm, 73 fs, 80 MHz) were split into two parts. One of them passed through a BBO crystal to produce the 408 nm pump pulses, while the other one was focused into a photonic crystal fiber (Newport SCG-800) to generate the supercontinuum white light. The probe was then selected with a 660 ± 10 nm bandpass filter (Thorlabs FB660-10). The spot size of the focused probe was about 1−2 μm. The delay time between pump and probe pulses was controlled by a steeper linear stage (Newport M-ILS150PP). To improve the signal-to-noise ratio, the reflected probe pulses passed through a 450 nm long-pass edge filter (Thorlabs FEL0450) and then were detected by a high-sensitivity photomultiplier (Thorlabs PMM02) connected with the phase lock-in amplifier (Stanford SR830).

Numerical Simulations. The full spatial-temporal dynamic model including multiexciton annihilation, ultrafast transition between exciton and trion, exciton−exciton annihilation, single-exciton recombination, and exciton diffusion was elaborately established (see Supporting Note S7 for more details). For the spatial distribution of exciton density, the model has an analytical solution of eq 1 owing to only the single-exciton recombination should be considered with exciton diffusion on the scale of several hundred picoseconds. To reproduce the experimental spatial emission profile (Figure 3c), the spatial distribution of exciton density was multiplied by an appropriate spatial distribution of PL efficiency per exciton and then convoluted with the instrument response function (see Supporting Note S8 for more details). For explaining the ultrafast signals in Figure 2e and f, the transition between exciton and trion was introduced. The modified rate equations 2a and 2b were numerically solved using the Runge−Kutta method to acquire the density evolution of the exciton and trion. Selecting an appropriate electron-doped concentration, Figure 2e and f were well fitted (see Supporting Note S9 for more details).

ASSOCIATED CONTENT

Supporting Information

The Supporting Information is available free of charge at https://pubs.acs.org/doi/10.1021/acsnano.0c01165.

Intrinsic modulated photoluminescence mappings and spectra under continuous wave excitation; intrinsic modulated Raman spectra; effects of high-fluence laser intensity; optical microscopy image of one CVD-grown ML MoS_2; remote lightening of edges for another sample; further confirmation of remote lightening phenomena; full spatial-temporal dynamic model of excitons; quantitative simulation of the spatial emission

https://dx.doi.org/10.1021/acsnano.0c01165
ACS Nano XXXX, XXX, XXX−XXX

profile; fitting of ultrafast relaxation at the first 10 ps; ultrafast transition between an exciton and trion for other sites; schematic of mirco-PL imaging apparatus (PDF)

Supporting Movie S1: Influences of excitation power on PL intensities of center region and edge region (AVI)

Supporting Movie S2: Spatial PL emission profiles for different excitation sites along the midperpendicular (AVI)

AUTHOR INFORMATION

Corresponding Author

Zheyu Fang − *School of Physics, State Key Laboratory for Mesoscopic Physics, Academy for Advanced Interdisciplinary Studies, Collaborative Innovation Center of Quantum Matter, Nano-optoelectronics Frontier Center of Ministry of Education, Peking University, Beijing 100871, China;* orcid.org/0000-0001-5780-0728; Email: zhyfang@pku.edu.cn

Authors

Pengfei Qi − *School of Physics, State Key Laboratory for Mesoscopic Physics, Academy for Advanced Interdisciplinary Studies, Collaborative Innovation Center of Quantum Matter, Nano-optoelectronics Frontier Center of Ministry of Education, Peking University, Beijing 100871, China;* orcid.org/0000-0003-2885-2072

Yang Luo − *School of Physics, State Key Laboratory for Mesoscopic Physics, Academy for Advanced Interdisciplinary Studies, Collaborative Innovation Center of Quantum Matter, Nano-optoelectronics Frontier Center of Ministry of Education, Peking University, Beijing 100871, China*

Wei Li − *Beijing Key Laboratory for Magnetoelectric Materials and Devices, Beijing Innovation Centre for Engineering Science and Advanced Technology, Department of Materials Science and Engineering, College of Engineering, Peking University, Beijing 100871, China*

Yang Cheng − *School of Physics, State Key Laboratory for Mesoscopic Physics, Academy for Advanced Interdisciplinary Studies, Collaborative Innovation Center of Quantum Matter, Nano-optoelectronics Frontier Center of Ministry of Education, Peking University, Beijing 100871, China*

Hangyong Shan − *School of Physics, State Key Laboratory for Mesoscopic Physics, Academy for Advanced Interdisciplinary Studies, Collaborative Innovation Center of Quantum Matter, Nano-optoelectronics Frontier Center of Ministry of Education, Peking University, Beijing 100871, China;* orcid.org/0000-0003-3988-4870

Xingli Wang − *CNRS International-NTU-Thales Research Alliance (CINTRA), Nanyang Technological University, Singapore 637553 Singapore*

Zheng Liu − *CNRS International-NTU-Thales Research Alliance (CINTRA), Nanyang Technological University, Singapore 637553 Singapore;* orcid.org/0000-0002-8825-7198

Pulickel M. Ajayan − *Department of Materials Science and NanoEngineering, Rice University, Houston, Texas 77005, United States;* orcid.org/0000-0001-8323-7860

Jun Lou − *Department of Materials Science and NanoEngineering, Rice University, Houston, Texas 77005, United States;* orcid.org/0000-0002-4351-9561

Yanglong Hou − *Beijing Key Laboratory for Magnetoelectric Materials and Devices, Beijing Innovation Centre for Engineering Science and Advanced Technology, Department of Materials Science and Engineering, College of Engineering, Peking University, Beijing 100871, China;* orcid.org/0000-0003-0579-4594

Kaihui Liu − *School of Physics, State Key Laboratory for Mesoscopic Physics, Academy for Advanced Interdisciplinary Studies, Collaborative Innovation Center of Quantum Matter, Nano-optoelectronics Frontier Center of Ministry of Education, Peking University, Beijing 100871, China*

Complete contact information is available at: https://pubs.acs.org/10.1021/acsnano.0c01165

Author Contributions

Z.F. supervised the project. P.Q. and Y.L. performed experiments and established the theoretical model. W.L., Y.C., Y.H., and K.L. carried out photoluminescence and Raman mappings. X.W., Z.L., P.M.A., and J.L. fabricated the samples. The manuscript was written through contributions of all authors. All authors have given approval to the final version of the manuscript.

Author Contributions

#P. Qi and Y. Luo contributed equally.

Notes

The authors declare no competing financial interest.

ACKNOWLEDGMENTS

This work is supported by the National Key Research and Development Program of China (2019YFA0210203, 2017YFA0205700, and 2017YFA0206000), National Science Foundation of China (11674012, 61521004, 21790364, 61422501, and 11374023), Beijing Natural Science Foundation (Z180011), Foundation for the Author of National Excellent Doctoral Dissertation of China (201420), National Program for Support of Top-notch Young Professionals (W02070003), and Project funded by China Postdoctoral Science Foundation (2019M660283).

REFERENCES

(1) Milnes, A. G. *Semiconductor Devices and Integrated Electronics*; Springer Science & Business Media: New York, 2012; p 505.

(2) Xu, Q.; Schmidt, B.; Pradhan, S.; Lipson, M. Micrometre-Scale Silicon Electro-Optic Modulator. *Nature* **2005**, *435*, 325−327.

(3) Kato, T.; Kaneko, T. Transport Dynamics of Neutral Excitons and Trions in Monolayer WS_2. *ACS Nano* **2016**, *10*, 9687−9694.

(4) Lundstrom, T.; Schoenfeld, W.; Lee, H.; Petroff, P. Exciton Storage in Semiconductor Self-Assembled Quantum Dots. *Science* **1999**, *286*, 2312−2314.

(5) Gärtner, A.; Holleitner, A.; Kotthaus, J.; Schuh, D. Drift Mobility of Long-Living Excitons in Coupled GaAs Quantum Wells. *Appl. Phys. Lett.* **2006**, *89*, No. 052108.

(6) Winbow, A. G.; Hammack, A. T.; Butov, L. V.; Gossard, A. C. Photon Storage with Nanosecond Switching in Coupled Quantum Well Nanostructures. *Nano Lett.* **2007**, *7*, 1349−1351.

(7) High, A.; Hammack, A.; Butov, L.; Hanson, M.; Gossard, A. Exciton Optoelectronic Transistor. *Opt. Lett.* **2007**, *32*, 2466−2468.

(8) High, A. A.; Novitskaya, E. E.; Butov, L. V.; Hanson, M.; Gossard, A. C. Control of Exciton Fluxes in an Excitonic Integrated Circuit. *Science* **2008**, *321*, 229−231.

(9) Grosso, G.; Graves, J.; Hammack, A.; High, A.; Butov, L.; Hanson, M.; Gossard, A. Excitonic Switches Operating at around 100 K. *Nat. Photonics* **2009**, *3*, 577−580.

(10) Moody, G.; Schaibley, J.; Xu, X. Exciton Dynamics in Monolayer Transition Metal Dichalcogenides. *J. Opt. Soc. Am. B* **2016**, *33*, C39−C49.

(11) Chernikov, A.; Berkelbach, T. C.; Hill, H. M.; Rigosi, A.; Li, Y.; Aslan, O. B.; Reichman, D. R.; Hybertsen, M. S.; Heinz, T. F. Exciton Binding Energy and Nonhydrogenic Rydberg Series in Monolayer WS_2. *Phys. Rev. Lett.* **2014**, *113*, No. 076802.
(12) Ugeda, M. M.; Bradley, A. J.; Shi, S.-F.; Felipe, H.; Zhang, Y.; Qiu, D. Y.; Ruan, W.; Mo, S.-K.; Hussain, Z.; Shen, Z.-X. Giant Bandgap Renormalization and Excitonic Effects in a Monolayer Transition Metal Dichalcogenide Semiconductor. *Nat. Mater.* **2014**, *13*, 1091−1095.
(13) He, K.; Kumar, N.; Zhao, L.; Wang, Z.; Mak, K. F.; Zhao, H.; Shan, J. Tightly Bound Excitons in Monolayer WSe_2. *Phys. Rev. Lett.* **2014**, *113*, No. 026803.
(14) Wang, G.; Chernikov, A.; Glazov, M. M.; Heinz, T. F.; Marie, X.; Amand, T.; Urbaszek, B. Colloquium: Excitons in Atomically Thin Transition Metal Dichalcogenides. *Rev. Mod. Phys.* **2018**, *90*, No. 021001.
(15) Schaibley, J. R.; Yu, H.; Clark, G.; Rivera, P.; Ross, J. S.; Seyler, K. L.; Yao, W.; Xu, X. Valleytronics in 2D Materials. *Nat. Rev. Mater.* **2016**, *1*, 16055.
(16) Mak, K. F.; He, K.; Shan, J.; Heinz, T. F. Control of Valley Polarization in Monolayer MoS_2 by Optical Helicity. *Nat. Nanotechnol.* **2012**, *7*, 494−498.
(17) Zeng, H.; Dai, J.; Yao, W.; Xiao, D.; Cui, X. Valley Polarization in MoS_2 Monolayers by Optical Pumping. *Nat. Nanotechnol.* **2012**, *7*, 490−493.
(18) Kim, J.; Hong, X.; Jin, C.; Shi, S. F.; Chang, C. Y. S.; Chiu, M. H.; Li, L. J.; Wang, F. Ultrafast Generation of Pseudo-Magnetic Field for Valley Excitons in WSe_2 Monolayers. *Science* **2014**, *346*, 1205−1208.
(19) Langer, F.; Schmid, C. P.; Schlauderer, S.; Gmitra, M.; Fabian, J.; Nagler, P.; Schüller, C.; Korn, T.; Hawkins, P.; Steiner, J. Lightwave Valleytronics in a Monolayer of Tungsten Diselenide. *Nature* **2018**, *557*, 76−80.
(20) Jin, C.; Kim, J.; Utama, M. I. B.; Regan, E. C.; Kleemann, H.; Cai, H.; Shen, Y.; Shinner, M. J.; Sengupta, A.; Watanabe, K. Imaging of Pure Spin-Valley Diffusion Current in WS_2-WSe_2 Heterostructures. *Science* **2018**, *360*, 893−896.
(21) Ye, Z.; Sun, D.; Heinz, T. F. Optical Manipulation of Valley Pseudospin. *Nat. Phys.* **2017**, *13*, 26−29.
(22) Feng, J.; Qian, X.; Huang, C.-W.; Li, J. Strain-Engineered Artificial Atom as a Broad-Spectrum Solar Energy Funnel. *Nat. Photonics* **2012**, *6*, 866−872.
(23) Li, H.; Contryman, A. W.; Qian, X.; Ardakani, S. M.; Gong, Y.; Wang, X.; Weisse, J. M.; Lee, C. H.; Zhao, J.; Ajayan, P. M. Optoelectronic Crystal of Artificial Atoms in Strain-Textured Molybdenum Disulphide. *Nat. Commun.* **2015**, *6*, 7381.
(24) Unuchek, D.; Ciarrocchi, A.; Avsar, A.; Watanabe, K.; Taniguchi, T.; Kis, A. Room-Temperature Electrical Control of Exciton Flux in a van der Waals Heterostructure. *Nature* **2018**, *560*, 340−344.
(25) Unuchek, D.; Ciarrocchi, A.; Avsar, A.; Sun, Z.; Watanabe, K.; Taniguchi, T.; Kis, A. Valley-Polarized Exciton Currents in a van der Waals Heterostructure. *Nat. Nanotechnol.* **2019**, *14*, 1104−1109.
(26) Hao, S.; Bellus, M. Z.; He, D.; Wang, Y.; Zhao, H. Controlling Exciton Transport in Monolayer $MoSe_2$ by Dielectric Screening. *Nanoscale Horiz.* **2020**, *5*, 139−143.
(27) Bao, W.; Borys, N. J.; Ko, C.; Suh, J.; Fan, W.; Thron, A.; Zhang, Y.; Buyanin, A.; Zhang, J.; Cabrini, S. Visualizing Nanoscale Excitonic Relaxation Properties of Disordered Edges and Grain Boundaries in Monolayer Molybdenum Disulfide. *Nat. Commun.* **2015**, *6*, 7993.
(28) Kim, M. S.; Yun, S. J.; Lee, Y.; Seo, C.; Han, G. H.; Kim, K. K.; Lee, Y. H.; Kim, J. Biexciton Emission from Edges and Grain Boundaries of Triangular WS_2 Monolayers. *ACS Nano* **2016**, *10*, 2399−2405.
(29) Huang, Y. L.; Chen, Y.; Zhang, W.; Quek, S. Y.; Chen, C.-H.; Li, L.-J.; Hsu, W.-T.; Chang, W.-H.; Zheng, Y. J.; Chen, W. Bandgap Tunability at Single-Layer Molybdenum Disulphide Grain Boundaries. *Nat. Commun.* **2015**, *6*, 6298.
(30) Li, H.; Zhang, Q.; Yap, C. C. R.; Tay, B. K.; Edwin, T. H. T.; Olivier, A.; Baillargeat, D. From Bulk to Monolayer MoS_2: Evolution of Raman Scattering. *Adv. Funct. Mater.* **2012**, *22*, 1385−1390.
(31) Li, Z.; Ye, R.; Feng, R.; Kang, Y.; Zhu, X.; Tour, J. M.; Fang, Z. Graphene Quantum Dots Doping of MoS_2 Monolayers. *Adv. Mater.* **2015**, *27*, 5235−5240.
(32) Irkhin, P.; Biaggio, I. Direct Imaging of Anisotropic Exciton Diffusion and Triplet Diffusion Length in Rubrene Single Crystals. *Phys. Rev. Lett.* **2011**, *107*, No. 017402.
(33) Onga, M.; Zhang, Y.; Ideue, T.; Iwasa, Y. Exciton Hall Effect in Monolayer MoS_2. *Nat. Mater.* **2017**, *16*, 1193−1197.
(34) Kulig, M.; Zipfel, J.; Nagler, P.; Blanter, S.; Schüller, C.; Korn, T.; Paradiso, N.; Glazov, M. M.; Chernikov, A. Exciton Diffusion and Halo Effects in Monolayer Semiconductors. *Phys. Rev. Lett.* **2018**, *120*, 207401.
(35) Cheng, J.; Jiang, T.; Ji, Q.; Zhang, Y.; Li, Z.; Shan, Y.; Zhang, Y.; Gong, X.; Liu, W.; Wu, S. Kinetic Nature of Grain Boundary Formation in As-Grown MoS_2 Monolayers. *Adv. Mater.* **2015**, *27*, 4069−4074.
(36) Castellanos-Gomez, A.; Roldán, R.; Cappelluti, E.; Buscema, M.; Guinea, F.; van der Zant, H. S. J.; Steele, G. A. Local Strain Engineering in Atomically Thin MoS_2. *Nano Lett.* **2013**, *13*, 5361−5366.
(37) Shan, H.; Yu, Y.; Zhang, R.; Cheng, R.; Zhang, D.; Luo, Y.; Wang, X.; Li, B.; Zu, S.; Lin, F. Electron Transfer and Cascade Relaxation Dynamics of Graphene Quantum Dots/MoS_2 Monolayer Mixed-Dimensional van der Waals Heterostructures. *Mater. Today* **2019**, *24*, 10−16.
(38) Shan, H.; Yu, Y.; Wang, X.; Luo, Y.; Zu, S.; Du, B.; Han, T.; Li, B.; Li, Y.; Wu, J. Direct Observation of Ultrafast Plasmonic Hot Electron Transfer in the Strong Coupling Regime. *Light: Sci. Appl.* **2019**, *8*, 9.
(39) Misra, S.; Stern, M.; Joshua, A.; Umansky, V.; Bar-Joseph, I. Experimental Study of the Exciton Gas-Liquid Transition in Coupled Quantum Wells. *Phys. Rev. Lett.* **2018**, *120*, No. 047402.
(40) Shiau, S.-Y.; Combescot, M. Optical Signature of Quantum Coherence in Fully Dark Exciton Condensates. *Phys. Rev. Lett.* **2019**, *123*, No. 097401.
(41) Najmaei, S.; Liu, Z.; Zhou, W.; Zou, X.; Shi, G.; Lei, S.; Yakobson, B. I.; Idrobo, J.-C.; Ajayan, P. M.; Lou, J. Vapour Phase Growth and Grain Boundary Structure of Molybdenum Disulphide Atomic Layers. *Nat. Mater.* **2013**, *12*, 754−759.
(42) Yu, Y.; Ji, Z.; Zu, S.; Du, B.; Kang, Y.; Li, Z.; Zhou, Z.; Shi, K.; Fang, Z. Ultrafast Plasmonic Hot Electron Transfer in Au Nanoantenna/MoS_2 Heterostructures. *Adv. Funct. Mater.* **2016**, *26*, 6394−6401.

https://dx.doi.org/10.1021/acsnano.0c01165
ACS Nano XXXX, XXX, XXX−XXX